Wrinkled surface topographies of electrospun polymer fibers

Lifeng Wang,[1] Chia-Ling Pai,[2] Mary C. Boyce,[1,a)] and Gregory C. Rutledge[2,a)]
[1]*Department of Mechanical Engineering, MIT, Cambridge, Massachusetts 02139, USA*
[2]*Department of Chemical Engineering, MIT, Cambridge, Massachusetts 02139, USA*

(Received 6 February 2009; accepted 20 March 2009; published online 17 April 2009)

Electrospun polymer fibers are shown to have wrinkled surface topographies that result from buckling instabilities during processing. A glassy shell forms on the surface of the gel-like core during solvent evaporation; continued evaporation leads to a contraction mismatch between the core and shell that triggers buckling of the shell. The wrinkled topographies are quantified in terms of the critical buckling wave number and wavelength. The results explain the observed wrinkled topographies and provide a framework for designing fibers with high specific surface areas and textured/patterned surface topographies to enhance surface dominated properties in fibers and fibrous mats. © *2009 American Institute of Physics*. [DOI: 10.1063/1.3118526]

Polymer fibers possessing diameters on the order of a few tens or hundreds of nanometers are readily produced by electrospinning and exhibit specific surface areas on the order of $1-100\ m^2/g$, much higher than bulk material or thin films. In addition to the generally expected circular cross section and smooth surface topology, a variety of cross-sectional shapes and corresponding surface textures have been observed,[1,2] as shown in the representative examples of Fig. 1. These include flat ribbonlike fiber geometries and wrinkled fiber surface topographies, which further increase the specific surface area and also provide a texture suitable for additional property enhancements. Figure 1(a) provides a scanning electron microscopy image of polystyrene (PS) fibers electrospun from a 30 wt % solution of amorphous, atactic PS (M_w=280 kg/mol) dissolved in tetrahydrofuran (THF). The inset transmission electron microscopy (TEM) image shows the corresponding cross section typical of these fibers. The ribbonlike morphology has a minor diameter of $\sim 2.1\ \mu m$ and a major diameter of $\sim 13.5\ \mu m$, and exhibits a wave number, defined as the number of maxima in radius around the perimeter (S) of the fiber cross section, of $k=2$ and wavelength $\lambda = S/k \sim 14\ \mu m$. Figure 1(b) shows images of polyacrylonitrile (PAN) fibers electrospun at 31% relative humidity (RH) from a 14 wt % solution of PAN (M_w =150 kg/mol) dissolved in dimethylformamide (DMF). The average fiber diameter is $1.35(\pm 0.21)\ \mu m$. These fibers exhibit a wrinkled topography with $k \sim 10$ and $\lambda \sim 400$ nm. Figure 1(c) shows images for PS fibers electrospun at 15% RH from a 30 wt % PS/DMF solution. The fiber diameter is $\sim 2.5\ \mu m$ with $k \sim 7$ and $\lambda \sim 1.1\ \mu m$, and bead diameter $\sim 5.2\ \mu m$ with $k \sim 12$ and $\lambda \sim 1.4\ \mu m$. Figure 1(d) shows images for PS fibers electrospun from a 15 wt % solution of PS dissolved in a mixed solvent of DMF and THF (1:1 by weight). The fibers exhibit beads-on-string morphology with fiber diameter $\sim 0.92(\pm 0.14)\ \mu m$ and maximum bead diameter $\sim 8.86(\pm 1.80)\ \mu m$. The cross-sectional TEM image in the inset shows a bead with $k \sim 16$ and $\lambda \sim 1\ \mu m$ (cutting the bead diameter at $\sim 3.8\ \mu m$ in this case, not necessarily at the maximum diameter).

Koombhongse *et al.*[1] proposed a mechanism for the formation of shaped fibers whereby atmospheric pressure tends to collapse the thin glassy skin initially formed on the liquid jet during solvent evaporation, giving a ribbonlike structure. Pauchard and Allain[3,4] and Pauchard and Couder[5] observed a similar phenomenon as a result of solvent evaporation from a sessile droplet of polymer solution. The collapse of the droplet leads to topographies that are qualitatively similar to the surface topographies observed in the beads of electrospun fibers [Fig. 1(d)]. The key to understanding this phenomenon is the buckling instability associated with the formation of a thin glassy skin (outer shell) on the surface of the fluid or gel-like core during processing. Solvent evaporation and drying lead to the rapid formation of a thin, elastic glassy shell. As solvent evaporation from the core proceeds, the core contracts and pulls radially inward on the shell, resulting in a compressive hoop stress in the shell. At a critical compressive stress, buckling of the shell is energetically favored over uniform circumferential compression. The favored buckling wavelength is that which results in the lowest total energy. The interplay between core and shell energy contributions is analogous to the classic problem of buckling of a beam on an elastic foundation: consideration of the elastic foundation strain energy leads to higher buckling modes being favored

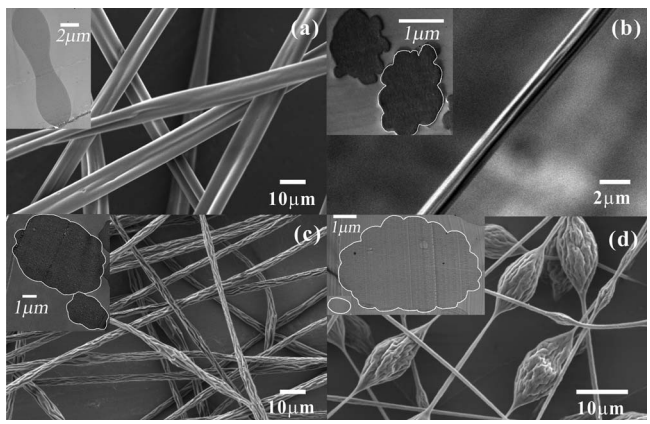

FIG. 1. Surface morphology of polymer fibers electrospun from (a) a 30 wt % PS/THF solution; (b) a 14 wt % PAN/DMF solution; (c) a 30 wt % PS/DMF solution; and (d) a 15 wt % PS in a mixed solvent of DMF and THF. Inset fibers outlined in white for emphasis.

a)Authors to whom correspondence should be addressed. Electronic addresses: mcboyce@mit.edu and rutledge@mit.edu.

over the lowest mode of the shell. Similar phenomena have been studied for thin films on compliant substrates[6–8] and spheroidal structures with layered core-shell structures.[9–11] Various deformation mismatch conditions have been found and/or used to trigger buckling, including deposition of a coating on a pretensioned elastomeric substrate followed by release of the pretension,[7,8] thermal expansion mismatch between a film and substrate,[9] and mismatch of either shrinkage or growth rates in multilayered structures (e.g., dehydration of vegetable and fruits,[10] growth of living plants[11]). We postulate the mechanism underlying the surface wrinkling of electrospun fibers to be a deformation mismatch between the shell and the core due to core shrinkage during solvent evaporation.

The critical buckling conditions of a long cylindrical elastic shell containing a compliant elastic core have been investigated in the context of the limiting external pressure of structural tubes.[12,13] The Herrmann and Forrestal[12] expression for the buckling pressure p of a shell as a function of buckling wave number k (for $k=2,3,4,\ldots$), shell properties and geometry (Young's modulus E_s, Poisson's ratio ν_s, and thickness t), and core properties and geometry (Young's modulus E_c, Poisson's ratio ν_c, and radius a) is given by

$$\frac{p}{p_0(1+\alpha)} = \frac{k^2-1}{3} + \frac{4(1-\nu_s^2)(E_c/E_s)(a/t)^3}{(1+\nu_c)[2k(1-\nu_c)-(1-2\nu_c)]}, \tag{1}$$

where $\alpha=(1-\nu_s^2)/[(1+\nu_c)(1-2\nu_c)](E_c/E_s)(a/t)$, $p_0=E_s/[4(1-\nu_s^2)](t/a)^3$.

The critical wave number k_{crit} corresponds to the k that gives the lowest buckling pressure according to Eq. (1). This approximate solution is accurate for values of core Poisson ratio between 0.4 and the incompressible limit of 0.5.[12] The Herrmann and Forrestal solution is applicable to our fiber system since the fiber gel-like core has a low shear modulus and a high bulk modulus, which corresponds to a Poisson's ratio close to 0.5. By minimizing Eq. (1) with respect to k and taking the limiting case of ν_c approaching 0.5, we obtain expressions for the critical wave number and wavelength,

$$k_{\mathrm{crit}} = (a/t)(3\bar{E}_c/\bar{E}_s)^{1/3}, \quad k_{\mathrm{crit}} \geq 2, \tag{2}$$

$$\lambda_{\mathrm{crit}} = 2\pi t(3\bar{E}_c/\bar{E}_s)^{-1/3}, \quad \lambda_{\mathrm{crit}} \leq \pi a, \tag{3}$$

where $\bar{E}=E/(1-\nu^2)$. The wave number is seen to scale with elastic property ratio via $(\bar{E}_c/\bar{E}_s)^{1/3}$ and linearly with a/t. The wavelength scales with $(\bar{E}_c/\bar{E}_s)^{-1/3}$, linearly with t, and for $\lambda_{\mathrm{crit}}<\pi a$, is independent of the radius a. When $a/t<2(3\bar{E}_c/\bar{E}_s)^{-1/3}$, the most favorable wavelength is limited by the circumference and hence $\lambda_{\mathrm{crit}}=\pi a$. The scaling of the wavelength with shell thickness and property ratios are consistent with those for wavy thin films on compliant substrates.[7,8] This consistency between the fiber and film wavelength scaling can be explained by simplified energy scaling and minimization arguments. For both the fiber and the film, the shell energy contribution (per unit length) is due to bending and scales as $\sim\bar{E}_s t^3 A^2/\lambda^4$, where A is the amplitude; the "foundation" energy contribution is due to straining that extends into the substrate (for film) or the core (for fiber) by a depth L_0 that scales with the wavelength $L_0\sim\lambda$, giving energy scaling as $\sim\bar{E}_c A^2/L_0$. Energy minimization then gives $\lambda\sim t(\bar{E}_s/\bar{E}_c)^{1/3}$, with λ being independent of radius and scaling in the same way as that of the film.[14]

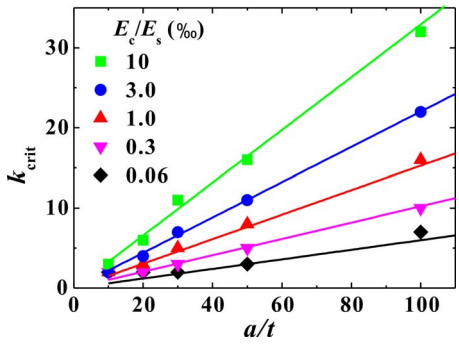

FIG. 2. (Color online) Dependence of critical wave number on a/t for different E_c/E_s. The lines are analytical results of Eq. (2); the symbols are numerical results.

Buckling patterns were further studied with nonlinear finite element analysis using ABAQUS/STANDARD.[15] Buckling modes were determined as follows. First, external pressure loading was assumed and an eigenanalysis was conducted to determine the critical wave number. Meshes were then "seeded" with infinitesimal amplitude of the critical mode. The core was then "contracted" to simulate solvent evaporation, leading to the radial mismatch condition that triggers buckling.

In Fig. 2, numerical and analytical results for the critical wave number k_{crit} as a function of a/t are shown for different E_c/E_s, and found to be in excellent agreement. At any given E_c/E_s, an increase in a/t gives an increase in k_{crit} that scales linearly with a/t; at any given a/t, an increase in E_c/E_s gives an increase in k_{crit} that scales with the cube root of E_c/E_s. Both trends reflect the increased energy penalty encountered in deforming a core of increasing stiffness, where the increase in k_{crit} optimally reduces the core strain energy.

Figure 3 shows a map of wrinkled topographies as a function of a/t (from 10 to 100) and E_c/E_s (from 0.06‰ to 10‰). The buckled conformations depict a core contraction of about 50%. This map provides a visual explanation of the wrinkled topographies observed in Fig. 1. For low E_c/E_s and low a/t, the core contraction provides relatively little energy penalty and hence the shell buckles in its lowest

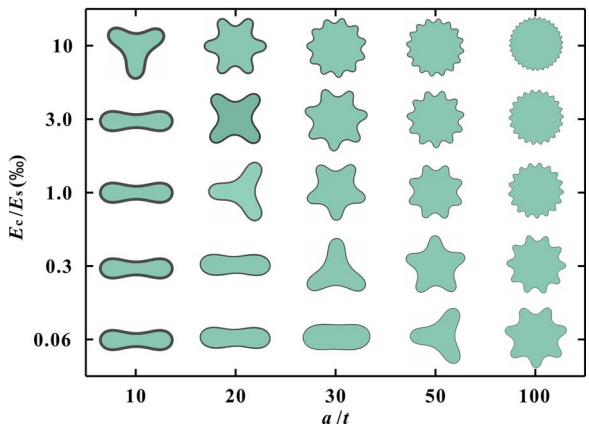

FIG. 3. (Color online) Map of numerical results for wrinkled cross-section as a function of E_c/E_s and a/t, shown for each pair of E_c/E_s and a/t values indicated by the axis labels.

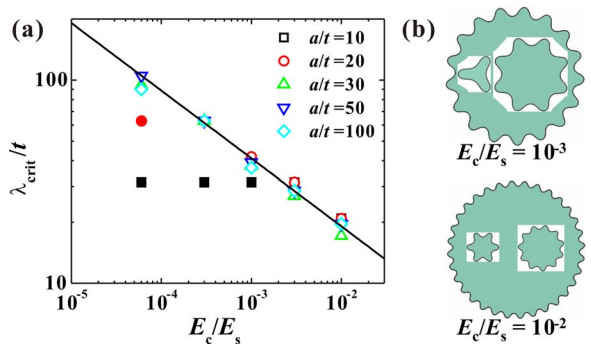

FIG. 4. (Color online) (a) Dependence of λ_{crit}/t on E_c/E_s for different a/t (solid line is the theory solution according to Eq. (3); filled symbols correspond to lowest mode cases where $k_{crit}=2$ and $\lambda_{crit}=\pi a$). (b) Surface patterns for different radius fibers with the same thickness t at $E_c/E_s=10^{-3}$ and $E_c/E_s=10^{-2}$, showing wavelength ($\lambda_{crit}=41t$ and $19t$, respectively) to be independent of fiber radius.

mode ($k=2$). As the core stiffness increases, either through increase in E_c/E_s or increase in a/t, the core energy penalty increases and the critical wave number k_{crit} increases. Furthermore, taking for instance the case of the beads-on-string morphology of Fig. 1(d), if we assume that the thickness of the polymer shell is uniform along the entire bead-on-string structure, then the small diameter of the string region corresponds to a small a/t and hence a smooth surface. Meanwhile, the diameter of the bead is about ten times larger than that of the fiber. Thus, the larger a/t of the bead results in a wrinkled topography with a large k_{crit} (between 7 and 32 from the map, depending on the relative properties E_c/E_s). (Here, the prolate spheroid geometry of the bead enabled use of the cylinder solution as an approximation to obtain the bead buckling conditions.[10]) This is consistent with the experimental observation of $k\sim16$.

The dependence of the critical buckling wavelength on E_c/E_s as obtained from the analytical model and the numerical simulations is shown in Fig. 4. Figure 4(a) plots λ_{crit}/t as a function of E_c/E_s for different a/t on a log plot. The analytical solution [Eq. (3)] indicates that λ_{crit}/t is independent of a/t and the numerical results are in agreement with this, with the exception of those cases where the wave number is 2 (i.e., the geometric limiting case of $\lambda_{crit}=\pi a$). λ_{crit}/t is shown to be an exponential function (with exponent$=-1/3$) of E_c/E_s, independent of a, except for the cases of low stiffness core where k_{crit} is 2. This indicates that when $k_{crit}>2$, the buckling wavelength is independent of a. This behavior is illustrated graphically in the topography results of Fig. 4(b), which show cross sections of three fibers with identical shell thickness but different radii. For the two cases of $E_c/E_s=10^{-3}$ and $E_c/E_s=10^{-2}$, one obtains $\lambda_{crit}=41t$ and $19t$, respectively. Note that for each E_c/E_s case, the wavelength is nearly the same (i.e., independent of a). Thus, for dry spinning processes such as electrospinning, where E_c/E_s is likely to be very small, the buckling wavelength can be tailored by manipulating the thickness of the shell, which can be easily achieved by controlling solvent volatility. This is illustrated by a comparison of Figs. 1(a) and 1(c). E_c/E_s is believed to be similar for these two cases since the polymer, molecular weight, and polymer concentration are the same for these two systems. Because THF is used in the system for Fig. 1(a), it evaporates more quickly than the DMF used in the system for Fig. 1(c). The thickness of the shell in Fig. 1(a) is thicker than Fig. 1(c), which manifests as the longer wavelength in Fig. 1(a) compared to Fig. 1(c). Conversely, it should be possible to estimate the shell thickness and hence to quantify the rate of solidification during the fiber forming process, from the mode number observed; a quantitative analysis to this effect, however, requires further experimental investigation. This effect can also be applied to core/shell fibers formed by coaxial electrospinning,[16] where selection of the core and shell fluids can potentially be used to tailor the surface topography of fiber or beads.

In conclusion, experimental, analytical, and numerical studies were carried out to investigate the wrinkled surface topographies of electrospun polymer fibers. The wrinkled or patterned topographies act to increase the specific surface area and to texture the surface, providing avenues for enhancing various attributes and properties of fibers and fibrous mats. For example, the hydrophobic nature of nonwoven mats can be enhanced because wrinkling imparts a second, finer scale roughness on top of the curved fiber surfaces. Some wrinkled fiber topographies contain axial grooves, which can act as capillary channels or fluid conduits such as those used in liquid chromatography. Conformal coating and/or functionalizing using chemical vapor deposition or layer-by-layer techniques can further enhance surface dominated properties.[17]

This research was supported by the U.S. Army through the Institute for Soldier Nanotechnologies (ISN), under Contract No. DAAD-19-02-D-0002. L.F.W. and C.L.P. contributed equally to this work.

[1] S. Koombhongse, W. Liu, and D. H. Reneker, J. Polym. Sci., Part B: Polym. Phys. **39**, 2598 (2001).
[2] C. L. Pai, M. C. Boyce, and G. C. Rutledge, Macromolecules **42**, 2102 (2009).
[3] L. Pauchard and C. Allain, Phys. Rev. E **68**, 052801 (2003).
[4] L. Pauchard and C. Allain, Europhys. Lett. **62**, 897 (2003).
[5] L. Pauchard and Y. Couder, Europhys. Lett. **66**, 667 (2004).
[6] L. Pocivavsek, R. Dellsy, A. Kern, S. Johnson, B. Lin, K. Y. C. Lee, and E. Cerda, Science **320**, 912 (2008).
[7] D. Y. Khang, H. Jiang, Y. Huang, and J. A. Rogers, Science **311**, 208 (2006).
[8] S. Wang, J. Song, D. H. Kim, Y. Huang, and J. A. Rogers, Appl. Phys. Lett. **93**, 023126 (2008).
[9] G. Cao, X. Chen, C. Li, A. Ji, and Z. Cao, Phys. Rev. Lett. **100**, 036102 (2008).
[10] J. Yin, Z. Cao, C. Li, I. Sheinman, and X. Chen, Proc. Natl. Acad. Sci. U.S.A. **105**, 19132 (2008).
[11] A. C. Newell, P. D. Shipman, and Z. Sun, J. Theor. Biol. **251**, 421 (2008).
[12] G. Herrmann and M. J. Forrestal, AIAA J. **3**, 1710 (1965).
[13] P. Seide, J. Aerospace Sci. **29**, 851 (1962).
[14] E. Cerda and L. Mahadevan, Phys. Rev. Lett. **90**, 074302 (2003).
[15] ABAQUS/STANDARD Version 6.6 Users' Manual, ABAQUS Inc., Providence, RI, 2006.
[16] J. H. Yu, S. V. Fridrikh, and G. C. Rutledge, Adv. Mater. **16**, 1562 (2004).
[17] M. Ma, M. Gupta, Z. Li, L. Zhai, K. K. Gleason, R. E. Cohen, M. F. Rubner, and G. C. Rutledge, Adv. Mater. **19**, 255 (2007).